Journal of Materials Chemistry A

PAPER

View Article Online
View Journal | View Issue

Cite this: J. Mater. Chem. A, 2017, 5, 24153

High-efficient electrocatalysts by unconventional acid-etching for overall water splitting†

Hao Wu, [abc] Ting Zhu, [abc] Xin Lu [abc] and Ghim Wei Ho *[abc]

Recent advances in doping and heterostructuring based on earth-abundant two-dimensional nanoframeworks provide new possibilities in electrocatalysis. In this study, a novel, unconventional, one-step self-regulating acid-etching strategy was developed to prepare two-tiered hierarchical Fe-doped and Pt-decorated nickel hydroxide nanosheets selectively for efficient oxygen evolution and hydrogen evolution reactions. The combinatorial hydrolysis of Ni ions in a self-limiting acidic environment induces selective growth of disparate dimension nanosheets. The proposed strategy, avoiding multifold structural design challenges, delivers highly exposed active sites and robust catalyst/support interfaces. Moreover, the exquisite structure and synergetic heterostructure modulation afford kinetically favorable electrolyte mass transport, and gas bubble release. Consequently, the structurally well-designed and hetero-coordinated electrodes attest highly efficient oxygen evolution with a low Tafel slope of 70.6 mV dec^{-1} and overpotential of 300 mV at a current density of 10 mA cm^{-2}, while it 30.4 mV dec^{-1} and 37 mV for hydrogen evolution, which rival performances of state-of-the-art electrocatalysts.

Received 7th October 2017
Accepted 30th October 2017

DOI: 10.1039/c7ta08826d

rsc.li/materials-a

Introduction

Two-dimensional (2D) earth-abundant nickel hydroxide-based nanomaterials are promising catalysts for electrochemical water splitting, because of their favorable electrochemical activity for both the oxygen evolution reaction (OER)[1–5] and hydrogen evolution reaction (HER).[6–8] Thus, it would be desirable to integrate overall water splitting using low-cost earth-abundant 2D nickel hydroxide-based electrocatalysts, especially in alkaline intermediates for amenable industrial requirements.[9–12] However, conventional synthetic protocols of insubordinate hydrolysis of Ni salts in alkaline conditions[13–19] result in notorious inferior conductivity and limited active sites. Two important areas for consideration are: (i) constructing elaborate frameworks especially those of hierarchical nano-geometries, offering high active surface areas, sufficient electrolyte permeation and favorable bubble release;[20–27] (ii) providing an intimate interface with superior electron transport and robust structure stability.[28–30]

Apart from structural constitution, rational design of materials composition is also crucial. The introduction of extrinsic dopant (*e.g.*, Fe) to nickel hydroxide has been conceived to enhance electrocatalytic OER activity by modulation of electronic structure that mediates a partial-charge-transfer mechanism.[31–33] Meanwhile, a synergistic nickel hydroxide/Pt scheme has been shown to boost HER activity in alkaline media, as reactive hydrogen intermediates (H_{ad}) are derived from effective water dissociation of the nickel hydroxides for efficient release of hydrogen on Pt surfaces.[6–8] However, the limited surface area of planar Pt substrate for depositing nickel hydroxides and the additional overpotential introduced by the Schottky barrier between the interfaces result in suboptimal catalytic performance.[6–8,34–36] Thus, there is great urgency to rationally design well-architectured and hetero-coordinated nickel hydroxide, which is central to high performance water electrolysis, using simple processing techniques.

Herein, an unconventional self-tuneable acid-etching strategy is proposed to prepare hierarchical two-tiered Fe-doped and Pt-decorated nickel hydroxide nanosheets in one step (Fig. 1). *In situ* etching of Ni, which simultaneously serves as an ion source and a support, results in superior interfacial contact, ensuring remarkable electrical conductance and structural stability. With the self-regulated pH environment, disparate dimensions of nanosheets are selectively synthesized and seamlessly stacked into two-tiered interlaced overlays producing an asymmetrical gradient porous structure. Importantly, the synthetic strategy conveniently incorporates trace amounts of heteroatom species (*i.e.* Fe and Pt) that markedly augment the chemical reactivity of the nickel hydroxide nanosheets. Notably, so far, no studies have been established focusing on such a facile *in situ* synthetic strategy to acquire hierarchical heterostructures for exceptional electrocatalytic

[a]Department of Electrical and Computer Engineering, National University of Singapore, 4 Engineering Drive 3, Singapore 117583. E-mail: elehgw@nus.edu.sg
[b]Engineering Science Programme, National University of Singapore, 9 Engineering Drive 1, Singapore 117575
[c]Institute of Materials Research and Engineering, A*STAR (Agency for Science, Technology and Research), 3 Research Link, Singapore 117602

† Electronic supplementary information (ESI) available. See DOI: 10.1039/c7ta08826d

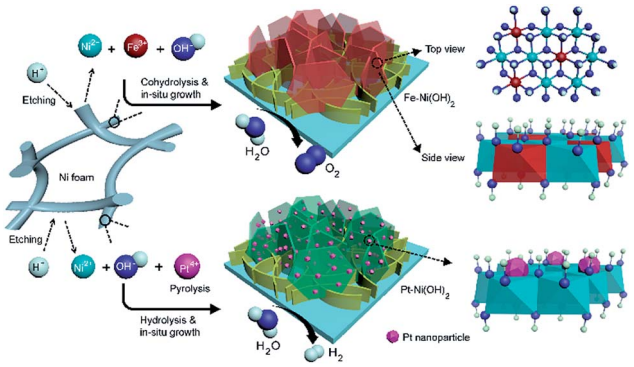

Fig. 1 Two-tiered Fe–Ni(OH)$_2$ and Pt–Ni(OH)$_2$ heterostructure synthesis and crystal configuration.

overall water splitting. With this established methodology, highly efficient and stable OER and HER electrodes with low Tafel slope and onset potential, high current density and large TOF are realized in alkaline intermediates. The proposed simple yet competent strategy, which exploits combinatorial hydrolysis of metal ions in self-regulated acid-etching, can be used to craft hierarchically stacked 2D nanosheets with electrochemical performance to rival that of state-of-the-art electrocatalysts. This rationally established strategy of self-regulated acid-etching has been extended successfully to design of other earth-abundant hierarchical metal hydroxide nanostructures.

Experimental

Chemicals

HCl, $Fe(NO_3)_3\cdot 9H_2O$, K_2PtCl_6, $Ni(NO_3)_2\cdot 6H_2O$, urea, NH_4F and NaOH were purchased from Sigma-Aldrich. All reagents were used as received without further purification.

Synthesis of hierarchical and Ni(OH)$_2$ nanosheets

To obtain hierarchically structured Ni(OH)$_2$ nanosheets, an *in situ* acidic wet etching method was developed. Firstly, a piece of Ni foam (5 cm × 1 cm, or Co foam to obtain hierarchical Co(OH)$_2$ nanosheets) was immersed in 1 M HCl with ultrasonic treatment to wash away the oxidation layer on the surface. Then, the Ni substrate was transferred to a sealed glass bottle with 0.11 mM HCl aqueous solution (20 ml) and heated to 80 °C under stirring for 20 h. The substrate was allowed to cool to room temperature naturally and washed with deionized (DI) water, followed by drying in an oven at 50 °C.

Synthesis of hierarchical Fe-doped Ni(OH)$_2$ nanosheets

For Fe–Ni(OH)$_2$ growth, a piece of HCl-treated Ni foam was treated as for the preparation of Ni(OH)$_2$ nanosheets with a mixture solution of 0.1 mM HCl and 0.01 mM $Fe(NO_3)_3\cdot 9H_2O$, and then procedures were followed as already described.

Synthesis of hierarchical Pt-decorated Ni(OH)$_2$ nanosheets

To prepare Pt–Ni(OH)$_2$ nanosheets, a piece of HCl-treated Ni foam was put into a mixed solution with 0.1 mM HCl and 0.01 mM K_2PtCl_6, and then procedures were followed as already described.

Synthesis of Ni(OH)$_2$ nanosheets

For comparison, a typical hydrothermal method was adopted as described in a previous work. In detail, Ni foam was firstly treated with HCl and then put into an autoclave with a mixture of 0.1 M $Ni(NO_3)_2\cdot 6H_2O$, 0.5 M urea and 0.2 M NH_4F. The hydrothermal process was conducted at 120 °C for 4 h, followed by DI water washing and then drying at 50 °C.

Characterization

Scanning electron microscopy (SEM) images were captured on a JEOL JSM-7001F field emission scanning electron microscope. High-resolution transition electron microscopy (HRTEM) images, energy-dispersive X-ray spectroscopy (EDX) and elemental mapping images were recorded using a JEOL JEM-2100 electron microscope. The X-ray diffraction (XRD) patterns were obtained on a Philips X-ray diffractometer with Cu Kα radiation. Tapping-mode AFM measurement was performed on a commercial SPM instrument (MPF-3D, Asylum Research, USA). XPS measurement was recorded on a Thermo Scientific ESCA Lab 250 spectrometer.

Electrochemical measurements. All electrochemical measurements were performed in a CHI 660E electrochemical workstation. All as-prepared substrates were directly used as working electrodes and tailored to 1 cm^2 in size. In three-electrode configuration, graphite rod and saturated calomel electrode (SCE) were used as the counter electrode and reference electrode, respectively. In two-electrode mode, Fe–Ni(OH)$_2$ and Pt–Ni(OH)$_2$ samples were set as anode and cathode, respectively. All tests were conducted in 1 M aqueous NaOH electrolyte. The measured potential was calibrated to RHE according to the following equation: $E_{RHE} = E_{SCE} + 0.245\ V + 0.059pH$. All polarization curves were recorded at a scanning rate of 1 mV s^{-1}, without *iR* compensation. Moreover, a Nafion membrane was used for blocking bubble diffusion during the gas collection process by a classical drainage method in the two-electrode mode. Notably, the gas collection operation started after 10 min of galvanostatic test at 40 mA cm^{-2} to expel the air in the bottles and was recorded at every further 1 ml of H_2 accumulation. The faradaic efficiency was calculated using the formula $\eta = zn/Q$, where z, n and Q represent the number of electron transfer, the amount of substance and the total power consumption, respectively. The turnover frequency for OER and HER was estimated following the equation: TOF $= jM/4Fm$ and TOF $= jM/2Fm$, where j is the current density, F is Faraday's constant (96 485.3C mol^{-1}), M is the molar mass, m is the loading mass, and numbers 4 and 2 means 4 and 2 electrons per mole of O_2 and H_2, respectively. The loading mass was estimated by assuming that all the reactants are fully converted into resultants.

Results and discussion

A mechanism for formation of two-tiered nickel hydroxide is proposed, of which the corresponding redox reactions are listed in the ESI.† In the initial stage, Ni at the near-surface is etched under a higher concentration of protons (pH ~4) to form Ni^{2+} ions, while only a trace amount undergo hydrolyzation to form the basal nickel hydroxide nanosheets. Subsequently, more concentrated Ni^{2+} ions are accessible to hydrolyze at a higher pH of ~6, resulting in formation of top-tiered nickel hydroxide nanosheets with a relatively large size. Hence, hierarchical two-tiered hydrolyzates are formed in a one-step tunable process. Trace amounts of heteroatom Fe and Pt species are introduced to optimize the electronic interaction and structure for enhancing OER and HER activity, respectively. Specifically, partial Fe^{3+} ions and the Ni^{2+} ions undergo cohydrolysis to form Fe-doped nickel hydroxides, because of their analogous solubility product constants.[16,17] For Pt coupling, Pt^{4+} ions are prone to decompose thermochemically to form metallic Pt on the nickel hydroxide, instead of hydrolyzing, because of the large solubility product constants of platinum(IV) ions.[6]

A uniform network composed of interwoven ultrathin nanosheets is observed for the H^+ etched sample, as viewed in SEM images (Fig. 2a–c, S1 and S2†). The morphologies of H^+/Fe^{3+} and H^+/Pt^{4+} etched samples for both sides are similar to those of H^+ etched ones (Fig. S3 and S4†). This implies the successful formation of hierarchical structures through the one-step *in situ* acid-etching methodology. The lateral size of the top-tiered nanosheets for H^+/Fe^{3+} and H^+/Pt^{4+} etched samples is ~1 μm, whereas it ~250 nm for the bottom tiers, respectively (Fig. S5†). Notably, the top tier nanosheets are intimately interfaced with the underlying tier (Fig. S6†), because of consecutive hydrolysis reactions that take place in a one-pot sequential environment and the homophase of nickel hydroxide. Extension of this strategy to use of Co foam (Fig. S7†) also results in a two-tiered nanosheet structure, further demonstrating the proposed formation mechanism and the universality of the self-regulating acid-etching methodology.

Composition of the co-etched nanosheets was identified subsequently by XRD patterns (Fig. 3a), where the main diffraction peaks are consistent with that of the pure H^+ etched one, and well matched with hexagonal β-$Ni(OH)_2$ (JCPDS no. 14-0117).[37] A TEM image of the H^+/Fe^{3+}-etched nanosheets, denoted as Fe–$Ni(OH)_2$, shows a well-defined 2D hexagonal sheet-like structure (Fig. 2d), and the corresponding SAED reveals the single-crystal characteristic of the individual nanosheet (Fig. 2e). The observed lattice fringe with interplanar spacing of ~0.28 nm (Fig. 2f) is consistent with the (110) plane of β-$Ni(OH)_2$ in the XRD results, while typical elemental mapping of Fe–$Ni(OH)_2$ nanosheet shows homogeneous doping of Fe (~1.7% to Ni) (Fig. S8 and S9†). Meanwhile, SEM and TEM of the H^+/Pt^{4+}-etched sample (designated as Pt–$Ni(OH)_2$) show also tiered ultrathin nanosheets but with incipient nanoparticles (~10 nm in size) (Fig. S10–S12†). The uniformly dispersed nanoparticles (~0.27% to Ni) with lattice spacing of ~0.22 nm are found to be the (111) plane of metallic Pt (Fig. S13†).

The Tyndall effect is observed for the Fe–$Ni(OH)_2$ nanosheet suspension (Fig. S14†), further reflecting its ultrathin character.[38] AFM was used to reveal the thickness of Fe–$Ni(OH)_2$ nanosheets (Fig. 3b), at only ~3 nm (6 single-unit-cell β-$Ni(OH)_2$ atomic layer) for a typical nanosheet. In contrast, $Ni(OH)_2$ nanosheet synthesized *via* a hydrothermal method[39] manifests a single-tier nanosheet structure with a much larger lateral size and thickness (~4 μm, Fig. S15†). It has been reported that materials of such confined thickness are more conductive than thicker ones, and this would be expected to improve the electrochemical properties.[37] XPS spectra further confirm the composition and element chemical state of the Fe–$Ni(OH)_2$ and

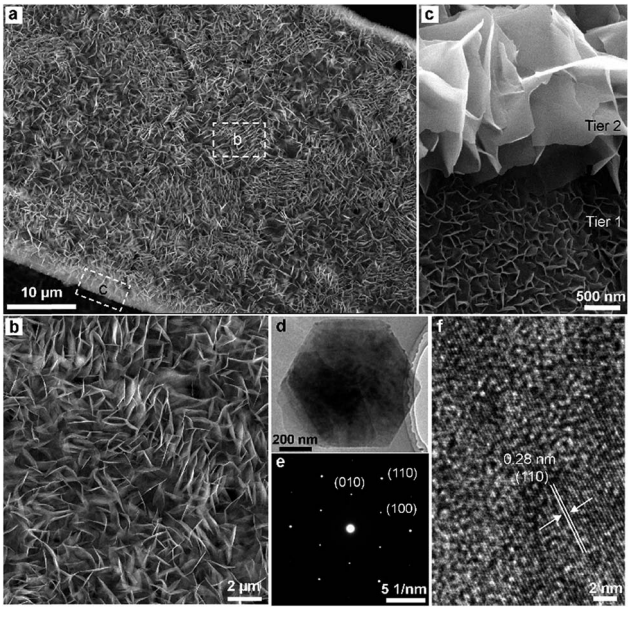

Fig. 2 (a, b) Scanning electron microscopy (SEM) images of $Ni(OH)_2$ nanosheets by acid-etching. (c) SEM image of two-tiered hierarchical $Ni(OH)_2$. (d–f) Transmission electron microscopy (TEM) image, corresponding selected-area electron diffraction (SAED) and high resolution (HRTEM) of Fe–$Ni(OH)_2$.

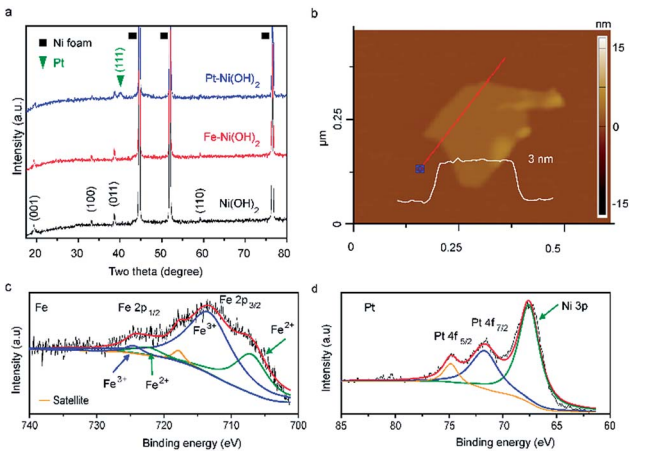

Fig. 3 (a) X-ray diffraction (XRD) patterns of $Ni(OH)_2$, Fe–$Ni(OH)_2$ and Pt–$Ni(OH)_2$. (b) AFM image of Fe–$Ni(OH)_2$, inset: height profile along the red curve. (c) XPS Fe 2p spectra of Fe–$Ni(OH)_2$. (d) Pt 4f spectra of Pt–$Ni(OH)_2$.

Pt–Ni(OH)$_2$ samples. Two sets of typical 2p peaks of Fe^{3+} (713.8 and 724.7 eV) and Fe^{2+} (707.4 and 722.9 eV)[17] ions of the Fe–Ni(OH)$_2$ sample further verify the successful incorporation and partial reduction of Fe^{3+} ions (Fig. 3c). For Pt–Ni(OH)$_2$, deconvoluted peaks located at 71.8 and 74.9 eV correspond well with the metallic Pt 4f spectra (Fig. 3d).[6] Peaks of O 1s for both samples reveal a high portion of adsorbed water (~27%),[40] suggestive of hydrophilic surfaces, which would benefit water electrolysis (Fig. S16 and S17†).

Oxygen evolution reaction behaviors, including polarization curves and relative Tafel plots, were determined for both hierarchical Ni(OH)$_2$ and Fe–Ni(OH)$_2$ nanosheets. Impressively, both the hierarchical Ni(OH)$_2$ and Fe–Ni(OH)$_2$ nanosheet electrodes show a much lower onset potential (1.48 V) than that of Ni(OH)$_2$ nanosheet (1.56 V) synthesized by a hydrothermal method, with the Ni foam hardly contributing to the OER activity (Fig. 4a). The current density of Fe–Ni(OH)$_2$ at 1.75 V is greatly improved from 160 to 290 mA cm^{-2}, with negligible decay after a stability test. The Tafel slope is enhanced from 94.2 to 70.6 mV dec^{-1} with a slight deterioration to 72.5 mV dec^{-1} after durability testing (Fig. 4b). These performances greatly surpass that of the nanosheet prepared by a hydrothermal method (137.8 mV dec^{-1}, Fig. S18†), revealing faster OER kinetics of the hierarchical nanosheets by the acid-etching approach. Remarkably, the two-tiered hierarchical electrode with gradient porous structure shows negligible gas bubble aggregation, whereas bubbles are extensively accumulated on the surface of one-tiered hydrothermal nanoflakes (Fig. S19†). The aerophobic nature of the two-tiered hierarchical nanosheets facilitates gas bubble release, further minimizing the overpotential for the electrocatalytic reactions.[23]

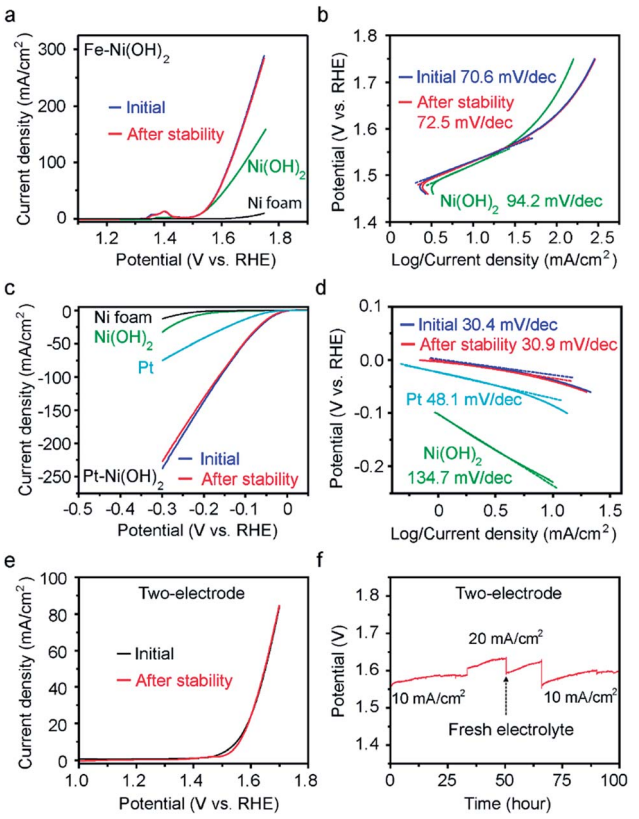

Fig. 4 (a) Linear sweep voltammetry (LSV) curves of Ni foam, Ni(OH)$_2$ and Fe–Ni(OH)$_2$ before and after stability test. (b) Corresponding Tafel plots. (c) LSV curves of Ni foam, Ni(OH)$_2$, Pt and Pt–Ni(OH)$_2$ before and after stability test. (d) Corresponding Tafel plots. (e) Two-electrode LSV curves (Fe–Ni(OH)$_2$ and Pt–Ni(OH)$_2$ as anode and cathode, respectively). (f) Two-electrode stability test.

Superior HER performance was also identified for the hierarchical Pt–Ni(OH)$_2$ nanosheet heterostructures, with an onset potential as low as −5 mV and a Tafel slope of 30.4 mV dec^{-1}, quite close to the theoretical value of Pt in acidic condition (29 mV dec^{-1}). This implies a Heyrovsky- or Tafel-determining step for HER (Fig. 4c and d).[35,36] Deliberately, one needs to enhance the surface areas of the catalysts and prohibit the bubble accumulation in order to accelerate the Heyrovsky or Tafel step,[36] which in this case has been explicitly ameliorated by the introduction of highly interconnected ultrathin nanosheets with non-symmetrical porous structure.[20,23] Distinctly, the Tafel slope decreases negligibly to 30.9 mV dec^{-1} after stability evaluation, which is far superior to the pure hierarchical Ni(OH)$_2$ nanosheet electrode (134.7 mV dec^{-1}), as well as the pure Pt foil (48.1 mV dec^{-1}) in alkaline electrolyte (Fig. S20†). Unambiguously, the notorious sluggish kinetics of the Volmer-step for the alkaline HER of Pt, has been promoted substantially with efficient H_2O dissociation through integration of the hierarchically tiered Ni(OH)$_2$ nanosheets.

Accordingly, the overall water splitting evaluation is performed with hierarchical Fe–Ni(OH)$_2$ and Pt–Ni(OH)$_2$ nanosheet as anode and cathode, respectively. The overpotential at 10 mA cm^{-2} is as low to 320 mV, only with 10 mV increment after stability test (Fig. 4e). The potential exhibits a slight increment (~2.5%) after 100 h continuous operation under the galvanostatic mode (Fig. 4f), and the morphologies for both electrodes are well maintained, indicating negligible deterioration of the two electrodes (Fig. S21†). Finally, a drainage system was adopted to collect the gases and evaluate the overall water splitting behavior in a more practical application (Fig. 5a). Impressively, the water electrolysis can be driven below 1.5 V using a Nafion membrane (Fig. 5b and c). With a current density of 40 mA cm^{-2} reached at ~2 V, the amount of H_2 and O_2 constantly evolves in a stoichiometric proportion of 2 : 1 (Fig. S22†). Acquisition of 12 ml H_2 is realized within ~43 min (corresponding to a H_2 production rate of ~0.75 mmol h^{-1}), with a faradaic efficiency of almost 100% (Fig. 5d and e).

Electrochemical surface area (ECSA),[5] being linearly proportional to the electrochemical double-layer capacitance, is used to estimate the accessible active sites for both electrodes (Fig. S23 and S24†). The corresponding values are calculated by considering all the surface areas to be active sites. The corresponding high ECSA of 10 and 29.8 mF cm^{-2} for the respective electrodes suggest vast active sites for efficient electrocatalytic reactions. The ECSA values show negligible decrease after stability test, again confirming their excellent durability. Besides the contribution of active sites, the TOF also plays a critical role in enhancing the intrinsic OER and HER activities.[41] As estimated, the TOF of hierarchical Fe–Ni(OH)$_2$ and

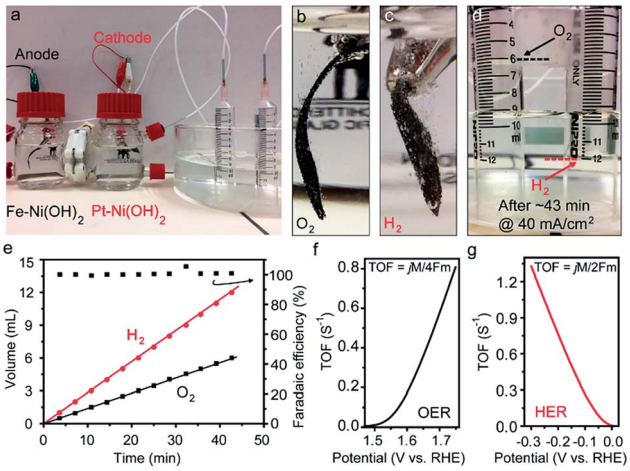

Fig. 5 (a) Two-electrode configuration for gas collection. (b, c) Gas bubble release on anode and cathode, respectively. (d) Gas collection of O_2 and H_2. (e) Gas volume *versus* time and corresponding faradaic efficiency. (f, g) TOF plots for OER and HER, respectively.

$Ni(OH)_2$ nanosheets for OER at 1.7 V are about 0.81 and 0.38 s^{-1}, much higher than that of hydrothermal $Ni(OH)_2$ (0.077 s^{-1}) (Fig. 5f and S25†). Meanwhile, the hierarchical Pt–$Ni(OH)_2$ nanosheet shows a TOF as high as 1.33 s^{-1} at −0.3 V, which is 8.5 times higher than that of hierarchical $Ni(OH)_2$, and 54 times higher than that of the hydrothermal nanosheet, demonstrating the predominance of the synergetic interaction of the hierarchical heterostructures in HER catalysis (Fig. 5g and S26†).

Additionally, the resistance between the interfaces, affecting the charge transfer kinetics, was investigated using EIS.[42,43] Nyquist plots of hierarchical Fe–$Ni(OH)_2$ clearly present a stable and low series resistance (R_s) and three charge transfer resistance (R_{ct}) and negligible R_{ct} between the two tiers, indicating a sturdy two-tiered structure (Fig. S27†). As a comparison, the hydrothermal one shows a comparable R_s but two R_{ct}, matching the single-tiered structure (Fig. S28†). For HER catalysis, the hierarchical $Ni(OH)_2$ electrode shows a low R_s but much smaller R_{ct} compared with the hydrothermal, revealing a preferable charge transfer of the hierarchically tiered structure (Fig. S29†). More importantly, the Pt–$Ni(OH)_2$ exhibits an additional but much smaller R_{ct}, resulting in negligible Schottky barriers between the interfaces that may improve substantially the kinetics of the Volmer-step for the alkaline HER catalysis (Fig. S30†).[32] Briefly, hierarchical nanostructures through acid-etching will facilitate charge transfer, and the heteroatom Fe and Pt incorporation further enhance the conductivity and the kinetics of gas production, thus resulting in high ECSA, excellent OER and record high HER (Tables S1 and S2†) catalytic properties.

Conclusions

In summary, an *in situ* self-regulating acid-etching methodology is proposed to acquire hierarchical 2D nickel hydroxide-based ultrathin nanosheets. Using this unconventional synthetic strategy, the nanosheet thickness can be controlled by the tuneable pH media and an elaborate two-tiered morphology can be established *via* a one-step facile process. Modification of the electronic structure by hetero species addition of Fe and Pt can yield unique hierarchical nanostructures with high-efficient OER and outstanding HER activity with low Tafel slope and onset potential, as well as high current density in alkaline intermediates. The proposed approach of combinatorial hydrolysis of metal ions in self-limiting acidic conditions to achieve hierarchical hydroxide nanostructures could pave the way for construction of desirable hierarchical metal hydroxide nanostructures for performance as exceptional catalysts.

Conflicts of interest

There are no conflicts to declare.

Acknowledgements

This research is supported by the National Research Foundation (NRF), under the Energy Innovation Research Programme (EIRP) R-263-000-B82-279, managed on behalf of the Building and Construction Authority (BCA).

References

1 C. McCrory, S. Jung, J. Peters and T. Jaramillo, *J. Am. Chem. Soc.*, 2013, **135**, 16977–16987.
2 M. Gong, Y. Li, H. Wang, Y. Liang, J. Wu, J. Zhou, J. Wang, T. Regier, F. Wei and H. Dai, *J. Am. Chem. Soc.*, 2013, **135**, 8452–8455.
3 M. Gao, W. Sheng, Z. Zhuang, Q. Fang, S. Gu, J. Jiang and Y. Yan, *J. Am. Chem. Soc.*, 2014, **136**, 7077–7084.
4 H. Liang, A. N. Gandi, C. Xia, M. N. Hedhili, D. H. Anjum, U. Schwingenschlögl and H. N. Alshareef, *ACS Energy Lett.*, 2017, **2**, 1022–1028.
5 H. Yin, S. Zhao, K. Zhao, A. Muqsit, H. Tang, L. Chang, H. Zhao, Y. Gao and Z. Tang, *Nat. Commun.*, 2015, **6**, 6430.
6 C. Xia, Q. Jiang, C. Zhao, M. N. Hedhili and H. N. Alshareef, *Adv. Mater.*, 2016, **28**, 77–85.
7 R. Subbaraman, D. Tripkovic, D. Strmcnik, K.-C. Chang, M. Uchimura, A. P. Paulikas, V. Stamenkovic and N. M. Markovic, *Science*, 2011, **334**, 1256–1260.
8 N. Danilovic, R. Subbaraman, D. Strmcnik, K.-C. Chang, A. P. Paulikas, V. R. Stamenkovic and N. M. Markovic, *Angew. Chem., Int. Ed.*, 2012, **51**, 12495–12498.
9 J. Luo, J.-H. Im, M. T. Mayer, M. Schreier, M. K. Nazeeruddin, N.-G. Park, S. D. Tilley, H. J. Fan and M. Grätzel, *Science*, 2014, **345**, 1593–1596.
10 W. Sheng, Z. Zhuang, M. Gao, J. Zheng, J. Chen and Y. Yan, *Nat. Commun.*, 2015, **6**, 5848.
11 H. Wang, Y. Hsu, R. Chen, T. Chan, H. Chen and B. Liu, *Adv. Energy Mater.*, 2015, **5**, 1500091.
12 X. Jia, Y. Zhao, G. Chen, L. Shang, R. Shi, X. Kang, G. I. N. Waterhouse, L.-Z. Wu, C.-H. Tung and T. Zhang, *Adv. Energy Mater.*, 2017, **7**, 1502585.
13 J. Xie, X. Zhang, H. Zhang, J. Zhang, S. Li, R. Wang, B. Pan and Y. Xie, *Adv. Mater.*, 2017, **29**, 1604765.

14 H. Liang, F. Meng, M. Cabán-Acevedo, L. Li, A. Forticaux, L. Xiu, Z. Wang and S. Jin, *Nano Lett.*, 2015, **15**, 1421–1427.
15 Z. Lu, H. Wang, D. Kong, K. Yan, P.-C. Hsu, G. Zheng, H. Yao, Z. Liang, X. Sun and Y. Cui, *Nat. Commun.*, 2014, **5**, 4345.
16 K. Fominykh, P. Chernev, I. Zaharieva, J. Sicklinger, G. Stefanic, D. Doblinger, A. Muller, A. Pokharel, S. Bocklein, C. Scheu, T. Bein and D. Fattakhova-Rohlfing, *ACS Nano*, 2015, **9**, 5180–5188.
17 X. Long, J. Li, S. Xiao, K. Yan, Z. Wang, H. Chen and S. Yang, *Angew. Chem., Int. Ed.*, 2014, **53**, 7584–7588.
18 F. Song and X. Hu, *Nat. Commun.*, 2014, **5**, 4477.
19 C. Chen, Y. Kang, Z. Huo, Z. Zhu, W. Huang, H. L. Xin, J. D. Snyder, D. Li, J. A. Herron, M. Mavrikakis, M. Chi, K. L. More, Y. Li, N. M. Markovic, G. A. Somorjai, P. Yang and V. R. Stamenkovic, *Science*, 2014, **343**, 1339–1343.
20 X. Lu and C. Zhao, *Nat. Commun.*, 2015, **6**, 6616.
21 S. Chen, J. Duan, P. Bian, Y. Tang, R. Zheng and S. Qiao, *Adv. Energy Mater.*, 2015, **5**, 1500936.
22 W. Lim, Y. Lim and G. W. Ho, *J. Mater. Chem A*, 2017, **5**, 919–924.
23 Z. Lu, W. Zhu, X. Yu, H. Zhang, Y. Li, X. Sun, X. Wang, H. Wang, J. Wang, J. Luo, X. Lei and L. Jiang, *Adv. Mater.*, 2014, **26**, 2683–2687.
24 M. Gong, W. Zhou, M.-C. Tsai, J. Zhou, M. Guan, M.-C. Lin, B. Zhang, Y. Hu, D.-Y. Wang, J. Yang, S. J. Pennycook, B.-J. Hwang and H. Dai, *Nat. Commun.*, 2014, **5**, 4695.
25 X. Cui, P. Xiao, J. Wang, M. Zhou, W. Guo, Y. Yang, Y. He, Z. Wang, Y. Yang, Y. Zhang and Z. Lin, *Angew. Chem., Int. Ed.*, 2017, **56**, 4488–4493.
26 S. Zhao, Z. Wang, Y. He, B. Jiang, Y. Harn, X. Liu, F. Yu, F. Feng, Q. Shen and Z. Lin, *ACS Energy Lett.*, 2017, **2**, 111–116.
27 H. Wang, S. Min, C. Ma, Z. Liu, W. Zhang, Q. Wang, D. Li, Y. Li, S. Turner, Y. Han, H. Zhu, E. Abou-hamad, M. N. J. Hedhili, J. Pan, W. Yu, K.-W. Huang, L.-J. Li, J. Yuan, M. Antonietti and T. Wu, *Nat. Commun.*, 2017, **8**, 13592.
28 Q. Lu, G. S. Hutchings, W. Yu, Y. Zhou, R. V. Forest, R. Tao, J. Rosen, B. T. Yonemoto, Z. Cao, H. Zheng, J. Q. Xiao, F. Jiao and J. G. Chen, *Nat. Commun.*, 2015, **6**, 6567.
29 D. Friebel, M. W. Louie, M. Bajdich, K. E. Sanwald, Y. Cai, A. M. Wise, M.-J. Cheng, D. Sokaras, T.-C. Weng, R. Alonso-Mori, R. C. Davis, J. R. Bargar, J. K. Nørskov, A. Nilsson and A. T. Bell, *J. Am. Chem. Soc.*, 2015, **137**, 1305–1313.
30 N. Li, D. K. Bediako, R. G. Hadt, D. Hayes, T. J. Kempa, F. Cube, D. C. Bell, L. X. Chen and D. G. Nocera, *Proc. Natl. Acad. Sci. U. S. A.*, 2017, **114**, 1486–1491.
31 L. Trotochaud, S. Young, J. Ranney and S. Boettcher, *J. Am. Chem. Soc.*, 2014, **136**, 6744–6753.
32 Y. Wang, L. Chen, X. Yu, Y. Wang and G. Zheng, *Adv. Energy Mater.*, 2017, **7**, 1601390.
33 N. Cheng, S. Stambula, D. Wang, M. N. Banis, J. Liu, A. Riese, B. Xiao, R. Li, T.-K. Sham, L.-M. Liu, G. A. Botton and X. Sun, *Nat. Commun.*, 2016, **7**, 13638.
34 R. Subbaraman, D. Tripkovic, K.-C. Chang, D. Strmcnik, A. P. Paulikas, P. Hirunsit, M. Chan, J. Greeley, V. Stamenkovic and N. M. Markovic, *Nat. Mater.*, 2012, **11**, 550–557.
35 L. Wang, C. Lin, D. Huang, J. Chen, L. Jiang, M. Wang, L. Chi, L. Shi and J. Jin, *ACS Catal.*, 2015, **5**, 3801–3806.
36 Z. Xing, C. Han, D. Wang, Q. Li and X. Yang, *ACS Catal.*, 2017, **7**, 7131–7135.
37 R. Wang, J. Lang, Y. Liu, Z. Lin and X. Yan, *NPG Asia Mater.*, 2015, **7**, e183.
38 M. Yang, Y.-J. Xu, W. Lu, K. Zeng, H. Zhu, Q.-H. Xu and G. W. Ho, *Nat. Commun.*, 2017, **8**, 14224.
39 H. Wu, M. Xu, H. Wu, J. Xu, Y. Wang, Z. Peng and G. Zheng, *J. Mater. Chem.*, 2012, **22**, 19821–19825.
40 H. Wu, J. Geng, H. Ge, Z. Guo, Y. Wang and G. Zheng, *Adv. Energy Mater.*, 2016, **6**, 1600794.
41 H. Wu, B. Xia, L. Yu, X. Yu and X. Lou, *Nat. Commun.*, 2015, **6**, 6512.
42 Q. Ding, J. Zhai, M. Cabán-Acevedo, M. J. Shearer, L. Li, H.-C. Chang, M.-L. Tsai, D. Ma, X. Zhang, R. J. Hamers, J.-H. He and S. Jin, *Adv. Mater.*, 2015, **27**, 6511–6518.
43 Q. Gong, Y. Wang, Q. Hu, J. Zhou, R. Feng, P. N. Duchesne, P. Zhang, F. Chen, N. Han, Y. Li and S.-T. Lee, *Nat. Commun.*, 2016, **7**, 13216.

